ARTICLE

Check for updates

Unveiling the ferrielectric nature of PbZrO$_3$-based antiferroelectric materials

Zhengqian Fu [1,6], Xuefeng Chen [2,6], Zhenqin Li [1,3], Tengfei Hu [1,4], Linlin Zhang[1], Ping Lu[1], Shujun Zhang [5], Genshui Wang [1,2✉], Xianlin Dong [1,2,4✉] & Fangfang Xu [1,4✉]

Benefitting from the reversible phase transition between antiferroelectric and ferroelectric states, antiferroelectric materials have recently received widespread attentions for energy storage applications. Antiferroelectric configuration with specific antiparallel dipoles has been used to establish antiferroelectric theories and understand its characteristic behaviors. Here, we report that the so-called antiferroelectric (Pb,La)(Zr,Sn,Ti)O$_3$ system is actually ferrielectric in nature. We demonstrate different ferrielectric configurations, which consists of ferroelectric ordering segments with either magnitude or angle modulation of dipoles. The ferrielectric configurations are mainly contributed from the coupling between A-cations and O-anions, and their displacement behavior is dependent largely on the chemical doping. Of particular significance is that the width and net polarization of ferroelectric ordering segments can be tailored by composition, which is linearly related to the key electrical characteristics, including switching field, remanent polarization and dielectric constant. These findings provide opportunities for comprehending structure-property correlation, developing antiferroelectric/ferrielectric theories and designing novel ferroic materials.

[1] State Key Laboratory of High Performance Ceramics and Superfine Microstructures, Shanghai Institute of Ceramics, Chinese Academy of Sciences, 200050 Shanghai, China. [2] The Key Lab of Inorganic Functional Materials and Devices, Shanghai Institute of Ceramics, Chinese Academy of Sciences, 200050 Shanghai, China. [3] University of Chinese Academy of Sciences, 100049 Beijing, China. [4] School of Physical Science and Technology, ShanghaiTech University, 201210 Shanghai, China. [5] Institute for Superconducting and Electronic Materials, Australian Institute of Innovative Materials, University of Wollongong, Wollongong, NSW 2500, Australia. [6] These authors contributed equally: Zhengqian Fu, Xuefeng Chen. ✉email: genshuiwang@mail.sic.ac.cn; xldong@mail.sic.ac.cn; ffxu@mail.sic.ac.cn

Dielectric capacitors have been commercialized for a wide range of applications including pulsed power systems, electrical vehicles, and medical devices[1–4]. Benefiting from the electrical field induced reversible phase transition between antiferroelectric (AFE) and ferroelectric (FE) states, AFE perovskite oxides (ABO_3) become promising candidate for dielectric energy storage capacitors due to their high power density, good energy storage density, and long lifetime[5–8].

Early in 1951, Kittel theoretically defined AFE configuration in analogy with antiferromagnetism as neighboring lines of dipoles pointing in antiparallel directions, while Sawaguchi et al. experimentally observed AFE behavior in $PbZrO_3$ ceramic according to its characteristic dielectric response and hysteresis loop[9,10]. Later on, the X-ray diffraction, neutron diffraction, convergent-beam electron diffraction, and high-resolution transmission electron microscopy have been applied to substantiate the AFE configuration in $PbZrO_3$[11–15]. Based on these comprehensive structural investigations, the basic dipoles ordering configuration of $PbZrO_3$ was established in which the two left-oriented dipole lines and two right-oriented dipole lines arrange alternately. Therefore, the $PbZrO_3$ has become the prototypical AFE material for understanding the physics of AFE and exploring new AFE materials. For AFE physics, theoretical models always involve ferrielectric (FiE) phase when AFE order parameter is coupled with field-induced polarization[16,17], while the FiE configuration has never been experimentally established. For AFE materials, numerous chemical elements (A-sites: La^{3+}, Ba^{2+}, Ca^{2+}, Sr^{2+}, etc.; B-sites: Sn^{4+}, Ti^{4+}, Nb^{5+}, etc.) have been attempted in $PbZrO_3$ for decreasing its extremely high switching field and optimizing energy storage characteristics[18–21]. As a consequence, the large family $PbZrO_3$-based solid solutions were considered as AFE materials with specific antiparallel polarization configuration, which has been rarely challenged.

In $PbZrO_3$-based ceramics, the chemical doping generally drives the AFE phase from commensurate structure to incommensurately modulated structure (IMS). The complex IMS was firstly investigated by MacLaren et al. in $(Pb_{0.96}La_{0.04})(Zr_{0.9}Ti_{0.1})_{0.99}O_3$ ceramics on atomic-scale, where the modulation of A-site cations was found to exist in a sinusoidal fashion[22]. Ma et al. further pointed out that the A-site cations were either antiparallel but imbalanced or in a nearly orthogonal arrangement in $(Pb_{0.99}Nb_{0.02}[(Zr_{0.57}Sn_{0.43})_{1-y}Ti_y]_{0.98}O_3$ ceramics[23]. These works have been regarded as an extraordinary step forward to the understanding of cation displacement in IMS. Nonetheless, early work has demonstrated that the prototypical $PbZrO_3$ showed multiple soft-mode vibrations, which mainly involved trilinear coupling between vibrations of Pb cations and librations of oxygen octahedra[24]. Moreover, the very recent work on the electron-beam illumination induced phase transition in $PbZrO_3$ single crystals clearly showed the hierarchical evolution of oxygen octahedra[25]. Thus, as an important component in perovskite $PbZrO_3$-based materials, the information of oxygen octahedra should be essentially taken into account for comprehending structure-property correlation and developing AFE/FiE theories.

Here, we use atomic-resolved scanning transmission electron microscopy to explore the electric dipoles ordering configurations in $(Pb,La)(Zr,Sn,Ti)O_3$ (PLZST) system, which is one of the most promising $PbZrO_3$-based AFE materials. We demonstrate the so-called AFE PLZST system has actual arrangement of dipoles in FiE configuration. The coupling between A/B-cations and O-anions is explicitly elucidated. Based on the FiE configurations, the key electrical properties can be clearly understood upon varying the composition.

Results

Characterization of average structure. $Pb_{0.97}La_{0.02}(Zr_{0.50}Sn_xTi_{0.50-x})O_3$ ceramics with $x = 0.50$, 0.45, 0.375 (hereafter denoted as PLZST 50/50/0, PLZST 50/45/5, and PLZST 50/37.5/12.5, respectively) were prepared by high temperature solid-state sintering method. X-ray diffraction studies reveal their crystal structures are periodically modulated because the characteristic superlattice reflections (marked by arrows) appear ahead of the {100} basic reflection (Fig. 1a, all crystallographic indices refer to the simple pseudocubic unit cell in this work). According to the crystal structure of $PbZrO_3$, these peaks are mainly associated with the displacement of cations. They gradually move upward to the {100} peaks indicating the modulation period (N_{IMS}) increases with decreasing Sn/Ti ratio. Combined with the selected area electron diffraction (SAED) patterns of [001], [100], and [1$\bar{1}$2] zone axes (Fig. 1b and Supplementary Fig. 1), it is confirmed that the modulation wave is along [110] direction with average N_{IMS} of 4.04, 6.15, and 9.37 for PLZST 50/50/0, PLZST 50/45/5, and PLZST 50/37.5/12.5, respectively (Fig. 1c). The fractional (irrational) values of N_{IMS} indicate that all three PLZST compositions show IMS. Meanwhile, the appearance of characteristic superlattice reflections associated with oxygen octahedral tilts in XRD (Fig. 1a, marked by dash rectangle) and [1-1.2] SAED patterns (Supplementary Fig. 1a, marked by blue arrow) indicates that the octahedra of PLZST have the similar antiphase tilt with $PbZrO_3$. It
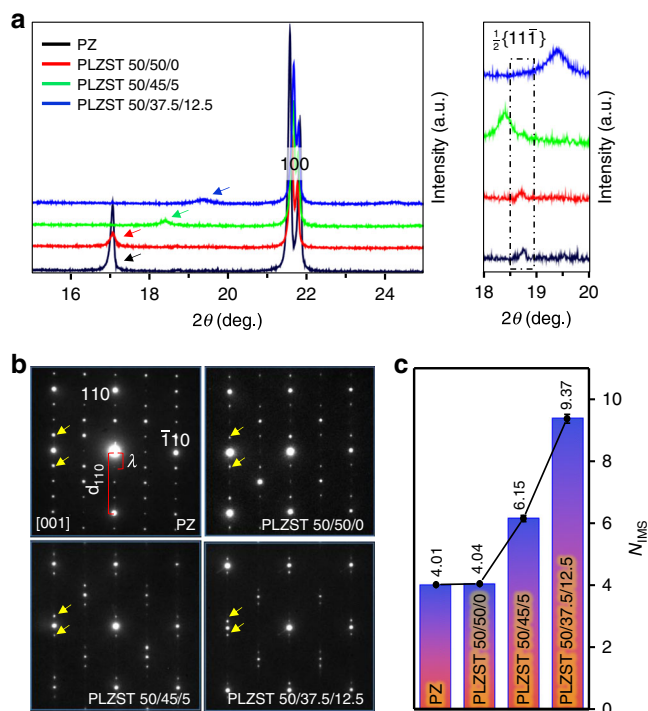

Fig. 1 Average structural characteristics of $PbZrO_3$ and PLZST system. a The XRD patterns showing two types of superlattice reflections originated from the cations modulation marked by arrows and octahedra tilts marked by dash rectangle, respectively. The 2θ range of 18°–20° are enlarged on the right to clearly show 1/2{11$\bar{1}$} peaks associated with antiphase tilt of oxygen octahedra. The main {100} peaks of $PbZrO_3$ is approximately aligned with PLZST 50/50/0 for clearly comparing modulation period. **b** The [001] SAED patterns showing the modulation wave along [110] direction. The satellite reflections associated with modulation mode are marked by yellow arrows. **c** The modulation period (N_{IMS}) = λ/d_{110} (λ refers to modulation wavelength in real-space) calculated from SAED patterns. The average data of modulation period for each sample is obtained from more than five different areas and error bars represent the standard deviation.

can be seen that the intensity of $1/2\{11\bar{1}\}$ reflections gradually decreases with decreasing Sn/Ti ratio. This implies the strong coupling of octahedra tilts with cations displacement, which is believed to stabilize the modulated structure[24,26,27] and will be further discussed in the following.

Atomic-scale analysis of modulated structure. Because spontaneous polarization (P_s) linearly relates with the atomic displacement, atomic-scale high-angle annular dark field (HAADF) imaging was performed to investigate the dipoles ordering configurations based on cations displacement in PLZST system. The picometer-precision fitting was applied to extract the cation column positions (see the details in Methods). Previous neutron diffraction studies on Zr-rich $Pb(Zr,Ti)O_3$ confirmed that Pb cations were responsible for the spontaneous polarization because the displacement magnitude of Pb cations was about three times that of Zr/Ti[28,29]. Similarly, it can be immediately accessible by directly observing the experimental HAADF images (Supplementary Fig. 2) that the A-site cations have obviously larger displacement than B-site cations in our PLZST system. Thus, we define the atomic displacement vectors (D_{AB}) as the relative offset of the A-site cations from the center of four adjacent B-site cations in the (001) plane. Displacement maps (Fig. 2) reveal that the dipoles are modulated periodically in all PLZST compositions, leading to the appearance of coherent fringes in medium-magnified TEM images (Supplementary Fig. 3). The modulation intervals are found to increase with decreasing Sn/Ti ratio, not necessarily only two dipole lines as modeled in the prototypical AFE configuration. The modulation structures are of incommensurate-type with fluctuant periods, which could be intuitively viewed from the width of dark/light-blue segments.
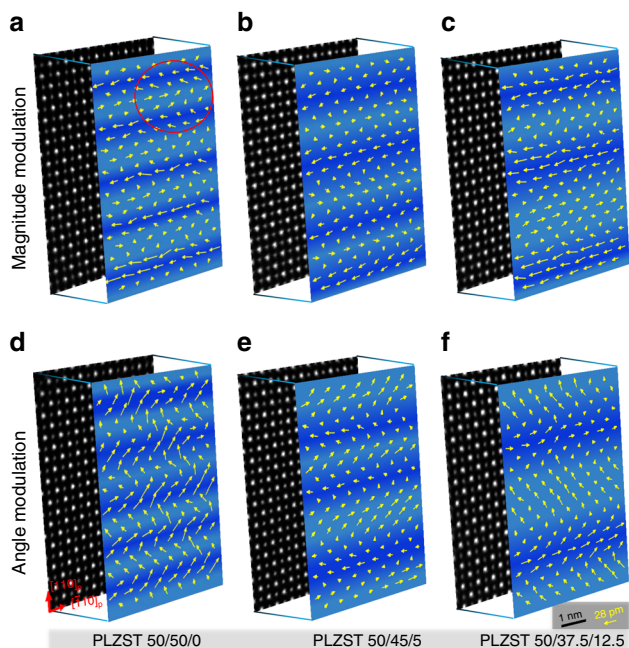

Fig. 2 Polarization mapping based on cations displacement in PLZST system. a–c Magnitude modulation mode and (**d–f**) angle modulation mode of dipoles ordering configurations (front) as revealed from the atomic-scale HAADF images (back) acquired along the [001] direction. The dark/light-blue backgrounds highlight the switch of polarization configuration. The full view of the corresponding HAADF images are presented in Supplementary Fig. 2. The red circled area in (**a**) shows the dipoles ordering configuration being nearly consistent with the one in $PbZrO_3$.

Interestingly, we observed two different modulation modes (either magnitude-type or angle-type) for each PLZST composition. In the magnitude modulation mode (Fig. 2a–c), all dipoles align nearly horizontally where the dark-blue segments exhibiting larger D_{AB} magnitude than the light-blue segments. On the other hand, in the angle modulation mode (Fig. 2d–f), the dipoles in the dark-blue segments and the light-blue segments have approximately equal D_{AB} magnitude but their orientations change alternately. In such case, it can be predicted that the net polarization should produce in both magnitude (in horizontal direction) and angle (in vertical direction) modulation modes. Therefore, we can conclude that the so-called AFE PLZST system essentially possesses ferrielectric (FiE) nature (also see the quantitative data in Supplementary Fig. 4). Based on the analysis for several areas in each PLZST composition, we found that the magnitude modulation mode was dominant and the two modulation modes could interchange freely (Supplementary Fig. 5). Besides, the polarization tends to be zero at the transitional area between dipole lines of different orientations (see the interface between dark-blue and light-blue segments), especially in the magnitude modulation mode. It can be noted that the PLZST 50/50/0 inherits the fourfold modulation period with some local areas approximately maintaining the dipoles ordering configuration of $PbZrO_3$ (e.g., the red circled area in Fig. 2a).

In order to explore the oxygen octahedral contribution to the observed FiE configuration and understand the coupling between O-anions displacement and A/B-cations displacement, atomic-scale annular bright field (ABF) imaging was applied to analyze the local structural characteristic of O-sublattice in the dominant modulation mode (Figs. 3 and 4). Similarly, the D_{AB} mappings (Fig. 3e–h) clearly show modulation of cation displacement as those observed in HAADF images (Fig. 2). It is generally accepted that the equally antiparallel D_{AB} collaborates with antiphase tilting of oxygen octahedra to stabilize the prototypical AFE structure in $PbZrO_3$. Actually, the distortion of oxygen octahedra should also have an important influence on the prototypical AFE structure, which can be clearly seen from the irregular shape of oxygen octahedra in Fig. 3a. The tilt and distortion of oxygen octahedra can be characterized by measuring the rippling of O-sublattice along x- and y-direction (Fig. 3i). Based on the experimental ABF images (Fig. 3b–d), we map the corner-shared BO_6 octahedra of PLZST system (Fig. 3j–l). The as-expected tilt and distortion of oxygen octahedra (see the irregular shape of oxygen octahedra and the rippling of O-row/column) was then found to occur simultaneously contributing to the observed FiE configuration in PLZST system. Interestingly, the coupling along x-direction is manifested by the modulation of y-rippling for O-sublattice, i.e., the large/small magnitude of D_{AB} usually corresponds to the high/low degree of y-rippling of O-rows (Fig. 3f–h, n–p), which can be understood by the Coulomb interaction (Supplementary Fig. 6). Thus, it can be understood that the decrease of intensity of $1/2\{11\bar{1}\}$ reflections in XRD (Fig. 1a) and SAED (Supplementary Fig. 1a) is caused by the increase of volume fraction of the areas with small y-rippling amplitude. Compared with the one in $PbZrO_3$ (Fig. 3m), it can be clearly seen that the y-rippling of O-rows in PLZST system breaks the long-rang antiphase octahedral tilt of $a^-a^-c^0$ system and is periodically modulated with local disorder.

Similarly, the coupling along y-direction can be manifested by the modulation of horizontal component of atomic displacement (Fig. 4). In $PbZrO_3$, the coupling features the characteristic that Zr-cations move in the same direction as Pb-cations while O-anions move in the opposite direction (Fig. 4a). In contrast, the coupling behavior in PLZST is strongly dependent on composition although displacement of both A/B-cation and O-anion are
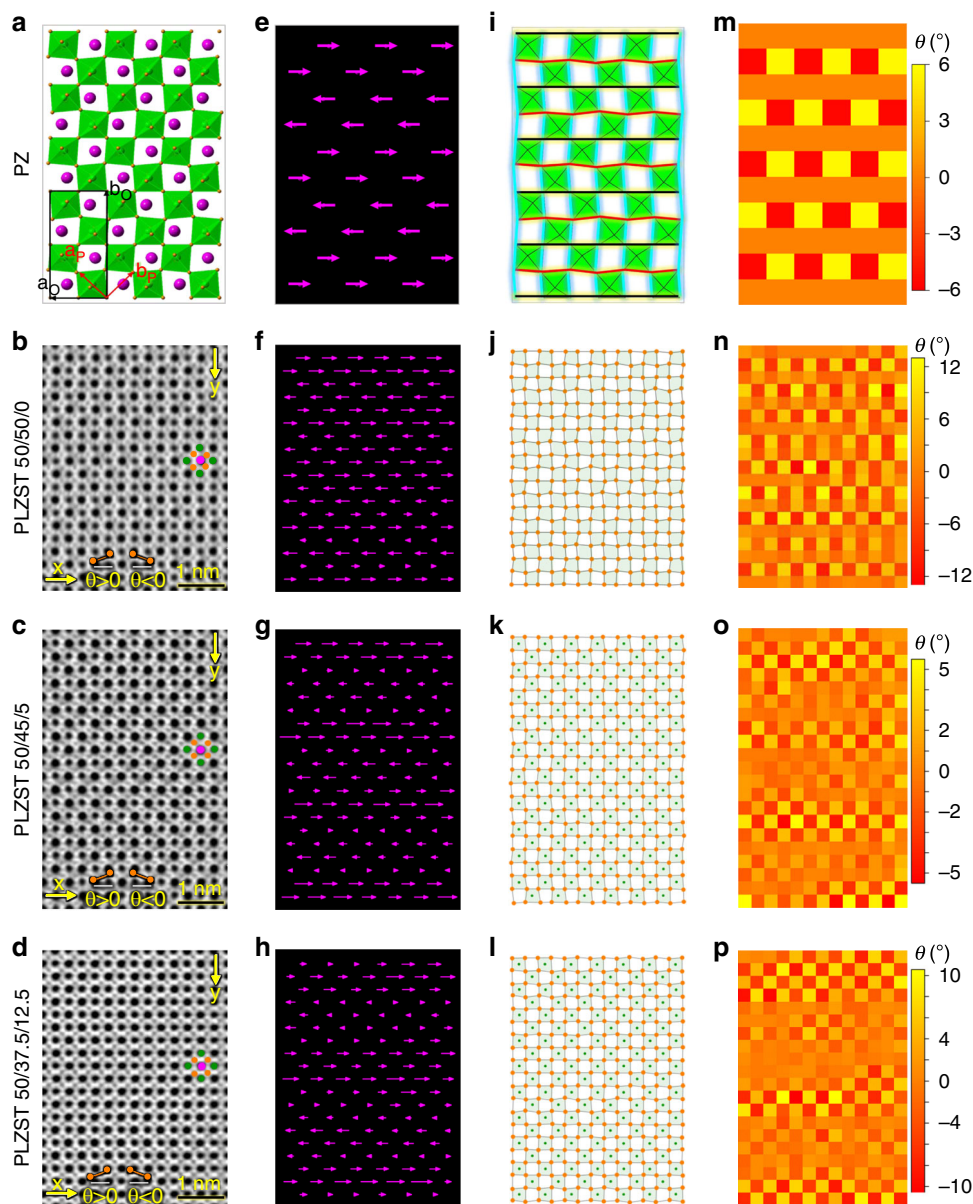
Fig. 3 Structural mapping of the coupling between O-anions displacement and A/B-cations displacement. a–d The $[001]_p$ projected structure of PbZrO$_3$ AFE phase (ref. [11]) and experimental ABF images of PLZST system, where purple, green, and orange balls represent A-cations, B-cations, and O-anions, respectively. The axis of "a_O/b_O" and "a_P/b_P" refer to orthorhombic and pseudocubic unit cell, respectively. The directions of "x/y" are defined as the $[\bar{1}10]_p/[\bar{1}\bar{1}0]_p$, respectively. The (**e–h**), (**i–l**), and (**m–p**) are the corresponding mappings of relative cations displacement ($\mathbf{D_{AB}}$), tilts and distortion of BO$_6$ octahedra, and y-rippling of O-sublattice, respectively. The black/red/cyan lines in (**i**) highlight the displacement behaviors of O-anions along x- and y-direction in PbZrO$_3$. The (**e–h**) only show the horizontal component of $\mathbf{D_{AB}}$ for clarity. The color scales represent local amplitude of y-rippling of O-sublattice, which is defined as Θ, i.e., the angle between O–O bond in a row and horizontal x-direction. The mapping of x-rippling of O-sublattice is not shown because it can be accessible in the corresponding quantitative profiles presented in Fig. 4.

modulated in corresponding period. Specifically, firstly, the PLZST 50/50/0 has a similar way to PbZrO$_3$, but there is a phase difference about one d$_{110}$ between A-cations and B-cations/O-anions (Fig. 4b). The horizontal displacement of O-anions in Fig. 4b refers to the data of odd column while its comparison to the displacement of even column and the sum of both columns are presented in Supplementary Fig. 7. Secondly, the PLZST 50/45/5 shows inverse behavior to PbZrO$_3$, i.e., B-cations move in the opposite direction to Pb-cations while O-anions move in accordance with A-site cations, synchronous alternation of large positive value and small negative value (Fig. 4c). Thirdly, the PLZST 50/37.5/12.5 presents nearly the same fashion as PbZrO$_3$,

in which the displacement of O-anions has approximately equal positive and negative value (Fig. 4d). Apart from the difference in coupling behavior, the displacement amplitude of both A/B-cation and O-anion gradually decrease with decreasing of Sn/Ti ratio, consequently led to the decrease of intensity of 1/2{11$\bar{1}$} reflections in XRD (Fig. 1a) and SAED (Supplementary Fig. 1) as well. Of particular interest is that the displacement of O-anion gradually changes its position with the reference of zero-line while the A-cations maintain the unbalanced displacement in all three compositions. Thus, the displacement of O-anion is also strongly affected by the doping effect of B-site elements. For instance, the stronger hybridization between B-cation and
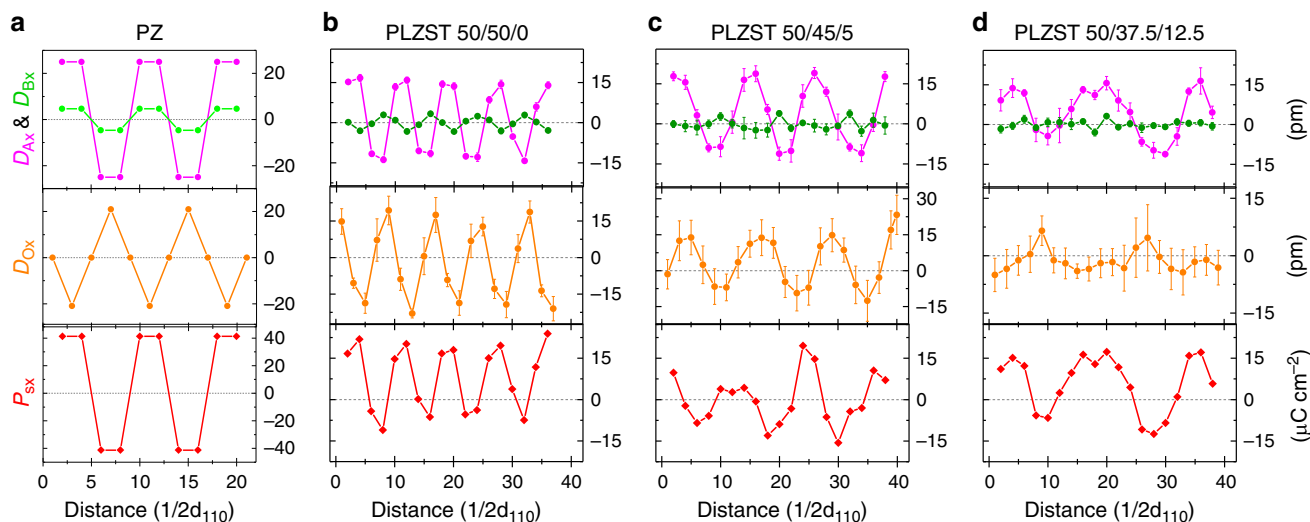
Fig. 4 Quantitative analysis of coupling between O-anions displacement and A/B-cations displacement. a–d The horizontal component of atomic displacement and spontaneous polarization for each atomic row is plotted as a function of distance along the y-direction for PbZrO$_3$ and PLZST system. The purple, green, orange, and red profiles represent the A-cations, B-cations, O-anions, and P_s, respectively. The value of these profiles are calculated from the Fig. 3a–d, where the displacement are defined as negative value when it aligns to the left. The corresponding profiles for vertical component are presented in Supplementary Fig. 8. The error bars represent the standard deviation measured from the experimental image.

O-anion occurs with higher Ti content in B-site (Zr/Sn/Ti) composition by taking account of difference in ionic radius and electronegativity.

Accompanied with the quantitative analysis of atomic displacement, the local polarization (Fig. 4 and Supplementary Fig. 8) is calculated in terms of standard definition $P_s = \frac{1}{V} \sum_i Z_i^* \delta_i$, where V, δ_i and Z_i^* are the volume of unit cell under consideration, atomic displacement with respect to the ideal position, and the Born effective charge, respectively. The Z_i^* values of cubic PbZrO$_3$ in ref. [30] are used for the PLZST system. Clearly, the horizontal $\mathbf{P_s}$ is also periodically modulated because of the main contribution from the displacement of A-cations and O-anions. The $\mathbf{P_s}$ of PLZST system have been substantially suppressed compared with PbZrO$_3$, especially in some local areas where structural disorder decreases the amplitude of the oxygen modulation. Thus, the O-anions should be taken into consideration for quantitative characterization of the polarization modulation. Nevertheless, the $\mathbf{P_s}$ profiles also presents the FiE configuration in all three PLZST compositions, being consistent with the quantitative $\mathbf{D_{AB}}$ mapping.

Structure–property correlation. According to the above structural characterizations, the interplay of FE, FiE, and AFE orderings and the structure-property relationship can be understood comprehensively. Figure 5 models the ideal FiE ordering configurations of PLZST system compared with the AFE ordering configuration of PbZrO$_3$. Here, only the dominant magnitude modulation mode is given for PLZST system. It should be noted that the dipoles ordering configurations in PLZST system actually have fluctuant periods and cyclic variation of magnitude, and in particular, the dipoles tend to be zero at the transitional area between dipole lines of different orientations (Figs. 2 and 4). Thus, the schematic illustrations with fixed modulated period and magnitude of dipoles in Fig. 5 are just the simplification of the experimental observations. Clearly, the AFE ordering originates from a couple of two-layer equivalent FE ordering segments with opposite directions (Fig. 5a) while the FiE ordering stems from two inversely polarized but nonequivalent FE ordering segments whose width is composition-dependent (Fig. 5b–d). The double/

multiple hysteresis loops are so inveterate for PbZrO$_3$-based materials that their AFE nature has been rarely challenged due to the similar polarization loops as observed in Fig. 5e. Nevertheless, some electric properties can hardly be understood based on prototypical AFE model. The FiE nature of PLZST system results in detectable remanent polarization (P_r), which increases linearly with the net polarization of FE segments (ΔP_s). It should be noted that although the measured ΔP_s value in the FiE region of PLZST 50/50/0 is obviously larger than the one in PLZST 50/45/5, the existence of large areas with AFE ordering (see Supplementary Fig. 9 and circled region in Fig. 2a) eventually results in an overall smaller P_r for PLZST 50/50/0. The modulation period (N_{IMS}) will increase by enlarging the FE ordering segments with decreasing the Sn/Ti ratio, i.e., 2 rows, 3 rows, and 5 rows for PLZST 50/50/0, PLZST 50/45/5, and PLZST 50/37.5/12.5, respectively, due to the fact that Ti favors the ferroelectricity while Sn favors the anti-ferroelectricity[19]. In this case, the interactions between the nearest neighboring dipoles with opposite direction will decrease, which will lead to the increased dielectric constant (ε_{RT}) and decreased forward switching field (E_{AF}), as shown in Fig. 5f and Supplementary Table 1. We also correlated N_{IMS} with P_r, ε_{RT} and E_{AF} in the Sr-doped PLZST system, where the similar trend was observed (Supplementary Fig. 10 and Supplementary Table 2), supporting the proposed correlation between modulation structure and macroscopic properties. Thus, the structure with anti-parallel, equal and narrow FE segments is highly desired for high energy storage application because it has low P_r and large forward switching field. This has been strongly evidenced in PLZST 50/50/0, which possesses the highest energy storage density of 9.82 J/cm^3 with satisfied energy efficiency of 84% (see the inset in Fig. 5e).

In summary, the current work determines the FiE nature of PLZST system, which has long been regarded as AFE materials. The FiE ordering originated from two unequal FE ordering segments with opposite directions (magnitude modulation) or two equal FE ordering segments with different orientations (angle modulation), which can be tailored by composition tuning, i.e., the Sn/Ti ratio in the studied PLZST system. The FiE ordering is mainly attributed to the coupling between A-cations and O-anions, which is strongly dependent on composition but has the
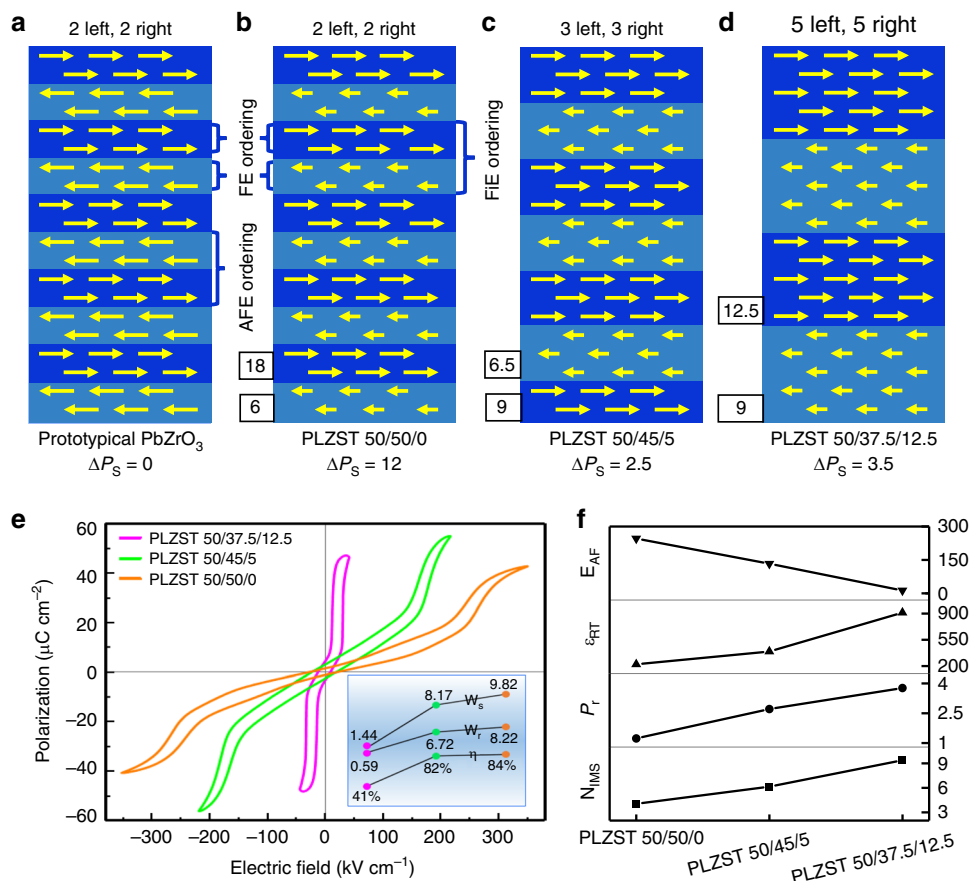
Fig. 5 Interplay of AFE, FiE, and FE ordering and structure–property correlation. a–d Ideal models of dipoles ordering configurations in PbZrO$_3$ and PLZST system. Arrows with left and right orientations represent the dipoles. The polarization value of FE segments in PLZST system is based on the quantitative data in Fig. 4. The ΔP_s refers to the net polarization of two adjacent FE segments (in unit of µC cm^{-2}). **e, f** Hysteresis loops, modulation period (N_{IMS}), remanent polarization (P_r, µC cm^{-2}), dielectric constant (ε_{RT}) and forward switching field (E_{AF}, kV cm^{-1}) of PLZST system. The inset in (**e**) shows the energy storage density (W_s, J cm^{-3}), recoverable energy density (W_r, J cm^{-3}) and energy efficiency (η) values.

common characteristics including, (a) both A-cations and O-anions are periodically modulated, breaking the long-range order of equally antiparallel cation displacement and antiphase octahedral tilt of the $a^-a^-c^0$ system in PbZrO$_3$; (b) the FE segments with large/small A-cations displacement correspond to the O-sublattice with high/low degree of y-rippling; (c) the tilt and distortion of oxygen octahedra simultaneously occur to stabilize the IMS. The relationship of composition, structure, and property has been established, providing a solid ground for materials design for numerous high/pulse power applications. In addition, the observation of FiE configurations is expected to motivate the exploration of AFE/FiE theories in perovskite oxides. Of particular importance is that, the chemical-driven dipole modulation, especially with large modulation period (Fig. 2f and Supplementary Fig. 5b), in PbZrO$_3$-based materials may open up additional opportunities for the emerging topological domains, such as flux-closure, polar vortices, and polar skyrmions[31–33], which up to now can only be obtained by epitaxial strain, while the coupling between epitaxial strain and chemical doping on the modulated dipole ordering configurations remains an open question.

Methods

Materials synthesis. Pb$_{0.97}$La$_{0.02}$(Zr$_{0.50}$Sn$_x$Ti$_{0.50-x}$)O$_3$ ceramics with $x = 0.50$, 0.45, 0.375 (hereafter denoted as PLZST 50/50/0, PLZST 50/45/5, and PLZST 50/37.5/12.5, respectively) were prepared by high temperature solid-state sintering method. Pb$_3$O$_4$, ZrO$_2$, TiO$_2$, La$_2$O$_3$, and SnO$_2$ powders with the purity of at least 99.0% were weighted and 0.5 wt% excess PbO were added to compensate for the volatilization

of Pb during sintering. Raw materials were ball-milled for 6 h and dried at 120 °C. Then they were calcined at 900 °C for 2 h. The PLZST powders were ball-milled again for 24 h, dried, mixed with 6 wt% PVA as binding agent and then pressed into pellets of 13 mm in diameter at 150 MPa. Finally, the binder was burnt out at 800 °C for 2 h and the pellets were sintered at 1300 °C for 2 h.

Electric properties characterization. All samples were polished to the thickness of 0.10–0.15 mm and the silver thin film was sputtered with the diameter of 0.75 mm as electrode. The room temperature polarization-electric field (P-E) hysteresis loops were characterized by aix ACCT TF 2000 analyzer FE measurement system (aix ACCT Co., Aachen, Germany) at 10 Hz and different electric fields.

X-ray diffraction. The X-ray diffraction were examined by an X-ray diffractometer (D/Max-2550V, Rigaku, Tokyo, Japan) with a Cu-Kα radiation. The slow scanning speed (time/step: 3 s per 0.005°) was set in order to clearly observe the superlattice reflections.

Transmission electron microscopy (TEM). TEM specimens were prepared by a conventional approach combining mechanical thinning and finally Ar + ion-milling in a Gatan PIPS II. The ion-milling voltage was gradually decrease from 3 keV to 0.5 keV to reduce ion-beam damage. Specimens were then coated with a thin-layer of carbon to minimize charging under the electron beams. The dark-field (DF) images and select-area electron diffraction (SAED) patterns were carried out on JEOL JEM-2100F microscope. The atomic-scale high-angle annular dark-field (HAADF) and annular bright-field (ABF) images were carried out on Cs-corrected JEOL JEM-ARM300F and Hitachi HF5000 microscopes. The experiment conditions were: probe size in 7C mode and convergence semi-angle of 18 mrad and collection semi-angle of 53–180 mrad (HAADF) and 10–20 mrad (ABF) for JEOL microscope; probe size in UHR mode and convergence semi-angle of 20 mrad and collection semi-angle of 60–320 mrad (HAADF) and 11–22 mrad (ABF) for Hitachi microscope.

The accurate and precise extraction of atomic column positions from HRSTEM images permits to quantify crystal structure parameters along the selected direction. In this case, the dipoles ordering configuration can be immediately accessible by direct imaging of the crystal structure. In this work, the picometer-precision fitting of atomic columns was done by MATLAB code, a least squares estimation algorithm for accurate and precise quantification of the atomic column positions and intensities with considering overlap between neighboring atomic columns, which has been used in previous literatures[34,35]. Considering the fact that the B-cations have very small displacement, the B-cations positions are averaged as reference points to calculate the displacement of A-cations, B-cations, and O-anions. The fitting of the atomic columns for A-cations, B-cations, and O-anions in this work has a 95% confidence interval of 4 pm, 3 pm, and 7 pm, respectively. The larger deviation of A-site columns than the one of B-site columns represents an overestimation of the precision of the fitting algorithm due to the modulated structure, which leads to a large fluctuation in distance between adjacent columns. Nevertheless, the polarization maps and profiles reveal the same evolution of modulation period with XRD (Fig. 1a), SAED (Fig. 1b and Supplementary Fig. 1) and modulation fringes (Supplementary Fig. 3), implying that the calculation results in this study are reliable and secure.

Data availability

The data that support the findings of this study are available from the corresponding author upon reasonable request.

References

1. Yao, Z. et al. Homogeneous/Inhomogeneous-structured dielectrics and their energy-storage performances. *Adv. Mater.* **29**, 1601727 (2017).
2. Pan, H. et al. Ultrahigh-energy density lead-free dielectric films via polymorphic nanodomain design. *Science* **365**, 578–582 (2019).
3. Wang, G. et al. Ultrahigh energy storage density lead-free multilayers by controlled electrical homogeneity. *Energy Environ. Sci.* **12**, 582–588 (2019).
4. Yang, L. et al. Perovskite lead-free dielectrics for energy storage applications. *Prog. Mater. Sci.* **102**, 72–108 (2019).
5. Hao, X., Zhai, J., Kong, L. B. & Xu, Z. A comprehensive review on the progress of lead zirconate-based antiferroelectric materials. *Prog. Mater. Sci.* **63**, 1–57 (2014).
6. Zhao, L., Liu, Q., Gao, J., Zhang, S. & Li, J. F. Lead-free antiferroelectric silver niobate tantalate with high energy storage performance. *Adv. Mater.* **29**, 1701824 (2017).
7. Wang, H., Liu, Y., Yang, T. & Zhang, S. Ultrahigh energy-storage density in antiferroelectric ceramics with field-induced multiphase transitions. *Adv. Funct. Mater.* **29**, 1807321 (2019).
8. Chen, M. J., Ning, X. K., Wang, S. F. & Fu, G. S. Significant enhancement of energy storage density and polarization in self-assembled PbZrO₃: NiO nano-columnar composite films. *Nanoscale* **11**, 1914–1920 (2019).
9. Kittel, C. Theory of antiferroelectric crystals. *Phys. Rev.* **82**, 729–732 (1951).
10. Shirane, G., Sawaguchi, E. & Takagi, Y. Dielectric properties of lead zirconate. *Phys. Rev.* **84**, 476–481 (1951).
11. Corker, D. L. et al. A Re-investigation of the crystal structure of the364 Perovskite PbZrO₃ by X-ray and Neutron Diffraction.*Acta Crystallogr B* **53**, 135–142 (1997).
12. Teslic, S. & Egami, T. Atomic structure of PbZrO₃ determined by pulsed neutron diffraction. *Acta Crystallogr B* **54**, 750–765 (1998).
13. Zhang, N. et al. A neutron diffuse scattering study of PbZrO₃ and Zr-rich PbZr1–xTixO₃. *J. Appl. Crystallogr.* **48**, 1637–1644 (2015).
14. Tanaka, M., Saito, R. & Tsuzuki, K. Determinations of space group and oxygen coordinates in the antiferroelectric phase of lead zirconate by conventional and convergent-beam electron diffraction. *J. Phys. Soc. Jpn.* **51**, 2635–2640 (1982).
15. Wei, X. K. et al. Ferroelectric translational antiphase boundaries in nonpolar materials. *Nat. Commun.* **5**, 3031 (2014).
16. Tolédano, P. & Guennou, M. Theory of antiferroelectric phase transitions. *Phys. Rev. B* **94**, 014107 (2016).
17. Tolédano, P. & Khalyavin, D. D. Symmetry-determined antiferroelectricity in PbZrO₃, NaNbO₃, and PbHfO₃. *Phys. Rev. B* **99**, 024105 (2019).
18. Shirane, G. Ferroelectricity and Antiferroelectricity in Ceramic PbZrO₃ Containing Ba or Sr. *Phys. Rev.* **86**, 219–227 (1952).
19. Berlincourt, D. Transducers using forced transitions between ferroelectric and antiferroelectric states. *IEEE Trans. Sonics Ultrason.* **13**, 116–130 (1966).
20. Lu, B. et al. Large electrocaloric effect in relaxor ferroelectric and antiferroelectric lanthanum doped lead zirconate titanate ceramics. *Sci. Rep.* **7**, 45335 (2017).
21. Zhuo, F. et al. Large field-induced strain, giant strain memory effect, and high thermal stability energy storage in (Pb,La)(Zr,Sn,Ti)O3 antiferroelectric single crystal. *Acta Mater.* **148**, 28–37 (2018).
22. MacLaren, I., Villaurrutia, R., Schaffer, B., Houben, L. & Peláiz-Barranco, A. Atomic scale imaging and quantification of electrical polarisation in incommensurate antiferroelectric lanthanum-doped lead zirconate titanate. *Adv. Funct. Mater.* **22**, 261–266 (2012).
23. Ma, T. et al. Uncompensated polarization in incommensurate modulations of perovskite antiferroelectrics. *Phys. Rev. Lett.* **123**, 217602 (2019).
24. Hlinka, J. et al. Multiple soft-mode vibrations of lead zirconate. *Phys. Rev. Lett.* **112**, 197601 (2014).
25. Wei, X. K. et al. An unconventional transient phase with cycloidal order of polarization in energy-storage antiferroelectric PbZrO₃. *Adv. Mater.* **32**, 1907208 (2020).
26. Tagantsev, A. K. et al. The origin of antiferroelectricity in PbZrO₃. *Nat. Commun.* **4**, 2229 (2013).
27. Lu, T. et al. Critical role of the coupling between the octahedral rotation and A-site ionic displacements in PbZrO₃-based antiferroelectric materials investigated by insitu neutron diffraction. *Phys. Rev. B* **96**, 214108 (2017).
28. Zhang, N., Yokota, H., Glazer, A. M. & Thomas, P. A. Neutron powder diffraction refinement of PbZr1-xTixO₃. *Acta Crystallogr B* **67**, 386–398 (2011).
29. Zhang, N. et al. The missing boundary in the phase diagram of PbZr1-xTixO₃. *Nat. Commun.* **5**, 5231 (2014).
30. Ghosez, P., Cockayne, E., Waghmare, U. V. & Rabe, K. M. Lattice dynamics of BaTiO₃, PbTiO₃, and PbZrO₃: a comparative first-principles study. *Phys. Rev. B* **60**, 836–843 (1999).
31. Tang, Y. L. et al. Observation of a periodic array of flux-closure quadrants in strained ferroelectric PbTiO₃ films. *Science* **348**, 547–551 (2015).
32. Yadav, A. K. et al. Observation of polar vortices in oxide superlattices. *Nature* **530**, 198–201 (2016).
33. Das, S. et al. Observation of room-temperature polar skyrmions. *Nature* **568**, 368–372 (2019).
34. De Backer, A. et al. StatSTEM: an efficient approach for accurate and precise model-based quantification of atomic resolution electron microscopy images. *Ultramicroscopy* **171**, 104–116 (2016).
35. Van Aert, S. et al. Advanced electron crystallography through model-based imaging. *IUCrJ* **3**, 71–83 (2016).

Author contributions

Z.F., F.X., G.W. and X.D. conceived the experiments. X.C. carried out the synthesis and electrical characterization. Z.F. and Z.L. did the atomic-scale HAADF and ABF experiments. T.H., P.L. and L.Z. performed SAED and XRD characterizations. F.X., S.Z., G.W., X.D., Z.F., and X.C. analyzed the data and co-wrote the paper. F.X., G.W. and X.D. supervised the research. All authors contributed to the discussions and paper preparation.

Competing interests

The authors declare no competing interests.

Additional information

Supplementary information is available for this paper at https://doi.org/10.1038/s41467-020-17664-w.

Correspondence and requests for materials should be addressed to G.W., X.D. or F.X.

Peer review information *Nature Communications* thanks Yuji Noguchi and Xiankui Wei for their contribution to the peer review of this work.

Reprints and permission information is available at http://www.nature.com/reprints

Publisher's note Springer Nature remains neutral with regard to jurisdictional claims in published maps and institutional affiliations.